Received: 20 July 2019 | Revised: 3 August 2020 | Accepted: 30 September 2020

DOI: 10.1002/stc.2652

WILEY

RESEARCH ARTICLE

A framework for hybrid simulation with online model updating suitable for hard real-time computing

Giuseppe Abbiati[1] | **Igor Lanese**[2] | **Saeed Eftekhar Azam**[3] | **Oreste S. Bursi**[4] | **Alberto Pavese**[5]

[1]Department of Engineering, Aarhus University, Aarhus, Denmark

[2]EUCENTRE - European Centre for Training and Research in Earthquake Engineering, Pavia (PV), Italy

[3]Department of Civil and Environmental Engineering, University of New Hampshire, Durham, New Hampshire, USA

[4]Department of Civil, Environmental and Mechanical Engineering, University of Trento, Trento, Italy

[5]Department of Civil Engineering and Architecture, University of Pavia, Pavia (PV), Italy

Correspondence
Giuseppe Abbiati, Department of Engineering, Aarhus University, Inge Lehmanns Gade 10, 8000 C Aarhus, Denmark.
Email: abbiati@eng.au.dk

Funding information
Horizon 2020, SERA project "Seismology and Earthquake Engineering Research Infrastructure Alliance for Europe", Grant/Award Number: 730900; Italian Ministry of Education, University and Research (MIUR), Department of Excellence, Grant/Award Number: L. 232/2016; Italian Ministry of Education, University and Research (MIUR), STRIT project "Strumenti e Tecnologie per la gestione del Rischio delle Infrastrutture di Trasporto"; Italian Civil Protection Department, Grant/Award Number: RELUIS-DPC 2014-2018 project; Experimental Laboratory of EUCENTRE, Pavia, Italy

Summary

The hybrid simulation method is used to test one or some components of a prototype structure subjected to a plausible loading history, accounting for their interaction with the untested ones, which are simulated numerically. If tested components have similar numerical counterparts, a possible approach to reduce simulation errors is to update the parameters of numerical substructures based on tested physical substructures. For this reason, online parameter estimation has gained the attention of the hybrid simulation community in the last decade. The term *online* indicates that the parameters of the identification model of the physical substructure are updated during the experiment. Main state-of-the-art middleware tools (e.g., OpenFresco and UI-SIMCOR) have been extended to support online model updating for the pseudodynamic hybrid simulation method. In this case, both numerical substructures and dynamic identification models are implemented on existing finite-element analysis software, which communicates with the middleware using a data exchange protocol with non-deterministic time schedule (e.g., TCP/IP). On the other hand, fast- and real-time hybrid simulation methods require a deterministic data exchange schedule between substructures, which imposes the adoption of hard real-time implementations. In this context, partitioned time integration is proposed to coordinate the parallel execution of simulation and model updating processes with heterogeneous sampling rates. As a result, the allocation of computational resources can leverage parallelization capabilities of multi-core CPUs.

KEYWORDS

hard real-time computing, hybrid simulation, online model updating, partitioned time integration, state-space modeling

1 | INTRODUCTION

1.1 | Background and motivation

The hybrid simulation (HS) method is used to test one or some components of a prototype structure (i.e., physical substructure [PS]) subjected to a plausible loading history, accounting for their interaction with the untested ones, which are simulated numerically (i.e., numerical substructure [NS]). Compared to shake table testing, it allows for the investigation of the experimental response of large or even full-scale structural prototypes with a reduced cost and effort.[1,2] A time integration algorithm coordinates the simulation by solving the equation of motion of the hybrid model. In detail, at each time step of the simulation loop, displacement and velocity predictors are calculated according to the selected time integration scheme. A set of servo-controlled actuators imposes displacement predictors to the PS and measures corresponding restoring forces while a structural analysis software computes the restoring force of the NS. Both PS and NS restoring force vectors enter the equation of motion of the hybrid model, which is typically solved without iterations by using an operator splitting approach or an explicit algorithm, and the simulation moves to the next time step. In order to reduce actuator control errors, if the PS restoring force is rate-independent, HS is performed with an extended time scale $\lambda = 20$–200 times slower than real-time, which corresponds to the so-called *pseudodynamic* regime. In this case, PS mass is also numerically simulated. An extended simulation time scale λ reduces the destabilizing effect of actuator lag, which is typical of the order of 10–20 ms. With the term *fast-time* HS, we refer to the testing time scale range $1 < \lambda < 20$, while *real-time* HS refers to the limit case of $\lambda = 1$.[3,4]

If the load resisting system of the prototype structure is composed of multiple substructures of equally uncertain behavior and the limited capacity of the experimental facility imposes to test only a few, model uncertainty inevitably affects some of the NSs and propagates to the hybrid model response. A possible approach to bound modeling error is to update the NS based on the response of the PS measured during the experiment. As explained in previous studies,[5,6] NS can be updated *online*, that is, during HS, based on the dynamic identification of similar PS experiencing larger excitation earlier. When this is not feasible, NS parameters can be updated *offline*, that is, in between subsequent tests (e.g., Abbiati et al.[7]).

In the field of online parameter estimation of the states of a hidden or partially observed process, Kalman filter is the most popular method for linear systems.[8] It is noteworthy that the online state-parameter estimation of a linear system turns into a nonlinear estimation problem. As an extension to nonlinear systems, the unscented Kalman filter (UKF) has attracted significant attention.[9] The main advantage of using the UKF is that the identification model is evaluated for a fixed number of sigma points. This is necessary to bound the time allocated for a single update of the state-parameter vector. Likewise, in the authors' knowledge, the UKF is the preferred choice for HS with online model updating (e.g., previous works[10–13]). The testing time scale determines the selection of a suitable architecture for the implementation of HS with online updating. Pseudodynamic HS usually relies on existing stand-alone finite-element (FE) software both for simulating the NS and the identification model of the PS. A middleware (e.g., OpenFresco[14] or UI-SIMCOR[15]) coordinates simulation and model updating (e.g., previous works[10–12]) using a non-deterministic communication protocol like the TCP/IP. On the other hand, real-time HS requires the exact synchronization of simulation, model updating, and control algorithms, which is attainable with a hard real-time computational platform. In real-time computing, the correctness of a task depends not only upon its logical correctness but also upon the time in which it is executed.[16] Accordingly, real-time systems are classified by the consequence of missing an execution deadline. Missing a deadline entails failure for *hard* real-time systems, whereas *firm* real-time systems tolerate infrequent deadline misses, but the usefulness of a result is zero after its deadline. The usefulness of a result degrades after its deadline for *soft* real-time systems. A hard real-time computational platform was used in Shao et al.[13] to enable real-time HS with online model updating. A similar architecture is proposed in Song and Dyke[17] to compute real-time model updating of hysteretic structural systems beyond the scope of HS. To avoid misunderstanding, when it accompanies HS, the adjective real-time refers to the testing time scale hereinafter. In all the other cases, real-time refers to the computational platform used to implement HS.

1.2 | Scope

Dynamic instability due to actuator tracking errors still prevents real-time HS from being adopted as a standard structural testing technique. In the authors' opinion, fast-time HS ($1 < \lambda < 20$) offers an appealing compromise between

stability and accuracy, which is often unexploited. If one adopts a pseudodynamic-like implementation architecture using both standard control system and testing equipment, it is reasonable to assume that the time needed to complete a simulation time step is about 50–100 ms of wall-clock time, including TCP/IP data exchange overhead. Accordingly, a testing time scale equal to 20 entails a delay of 2.5–5.0 ms in simulation time, which is a lot if compared to a typical time integration step of 1 ms. Reducing delay to sole actuator lag requires a hard real-time implementation, for example, based on MATLAB xPC Target.[18] In this case, the common practice of coordinating simulation and model updating with a monolithic time integration algorithm does not exploit multi-rate code parallelization capabilities of modern multi-core CPUs. Partitioned time integration instead allows for parallelizing simulation and model updating tasks over different CPU cores using heterogeneous sampling rates. The computational overhead associated with the coordination of the HS is negligible and limited to the calculation of interconnecting forces among substructures obtained with the solution of a linearized interface problem.[19,20]

Building upon a state-space partitioned time integration algorithm developed by some of the authors,[21] this paper illustrates a scalable multi-rate multi-core implementation architecture for HS with online model updating. The main advantage is that the simulation of NS and dynamic identification of PS can be parallelized and solved with a sampling period at least λ times larger than the one adopted for solving the PS response. Accordingly, the complexity of simulation and identification models can be adjusted based on the testing time scale. Moreover, PS interconnecting forces obtained from the solution of the linearized interface problem do not require further post-processing of input loading for dynamic identification.

The paper is organized as follows. Section 2 describes the developed HS framework. Section 3 presents a verification case study consisting of a three-span reinforced concrete (RC) bridge subjected to seismic loading. The main results of HS experiments are reported and commented in Section 4. Finally, conclusions and future developments are drawn in Section 5.

2 | DESCRIPTION OF THE HYBRID SIMULATION FRAMEWORK

2.1 | Time integration and online model updating algorithms

The seminal report of Pegon and Magonette[22] describes the first use of partitioned time integration for *pseudodynamic* HS. The original purpose was to eliminate restoring force relaxation associated with the hold phase of the experimental load step procedure. In principle, PS and NS responses are solved by two separate monolithic time integration processes with heterogenous time steps. A smaller time step is used to compute the PS response, which is sampled at the same rate of the actuator control system thus avoiding ramp-and-hold phases. A coarser time step is used for solving the NS response, which may require to communicate with external FE software. In this regard, the term *subcycling* indicates that the time step size adopted for the NS is a multiple of the time step size adopted for the PS. Coupling of PS and NS is enforced by a set of self-balanced interconnecting forces represented by Lagrange multipliers, which are obtained by the solution of a linearized interface problem. As a result, the coordination of the HS relies upon a single matrix multiplication. A detailed analysis of the algorithm proposed by Pegon and Magonette is reported in Bonelli et al.[19] A comprehensive description of the experimental implementation for testing an RC bridge is summarized in Bursi et al.[20]

Building upon the idea of decimating the NS response, which is a dual interpretation of subcycling the PS response, and leveraging on the reduced computational effort required for coordinating the HS, a state-space partitioned time integration scheme was developed by some of the authors to enable fast-time HS with nonlinear NSs.[21] The Partitioned-Generalized-α (PG-α) time integration scheme coordinates two Monolithic-Generalized-α (MG-α) time integrator schemes[23] by using the coupling scheme of the modified PH method.[24] The state-space paradigm was selected to facilitate the implementation of nonlinear NSs based on phenomenological hysteretic models (e.g., previous studies[25,26]), which are suitable for hard real-time computing. For a generic substructure, the state-space equation of motion reads

$$\mathbf{M}\dot{\mathbf{Y}} + \mathbf{R}(\mathbf{Y}) = \mathbf{F}(t), \tag{1}$$

with

$$\mathbf{Y}=\begin{bmatrix}\mathbf{u}\\ \mathbf{v}\\ \mathbf{s}\end{bmatrix},\mathbf{M}=\begin{bmatrix}\mathbf{I} & \mathbf{0} & \mathbf{0}\\ \mathbf{0} & \mathbf{m} & \mathbf{0}\\ \mathbf{0} & \mathbf{0} & \mathbf{I}\end{bmatrix},\mathbf{R}=\begin{bmatrix}-\mathbf{v}\\ \mathbf{r}(\mathbf{u},\mathbf{v},\mathbf{s})\\ \mathbf{g}(\mathbf{u},\mathbf{v},\mathbf{s})\end{bmatrix},\mathbf{F}(t)=\begin{bmatrix}\mathbf{0}\\ \mathbf{f}(t)\\ \mathbf{0}\end{bmatrix}. \tag{2}$$

In detail, **u**, **v**, and **s** are displacement, velocity, and additional state variables, respectively. The former two always appear as a pair in second-order mechanical systems, while the latter is used to model nonlinearities endowed with memory (e.g., hysteresis). In particular, **r**(**u**,**v**,**s**) is the nonlinear restoring force vector while the nonlinear function **g**(**u**,**v**,**s**) models the evolution of the additional state variables **s**. Finally, **m** is the mass matrix, and **f**(t) is the external time-varying load while **I** and **0** are respectively identity and zero matrices with appropriate dimensions. For simplicity of the notation, time dependency is omitted, and **M**, **R**, and **F** are referred to as generalized mass, restoring force, and external loading. The corresponding coupled equations of motion of NS and PS solved by the PG-α scheme read

$$\begin{cases}\mathbf{M}^N\dot{\mathbf{Y}}^N_{n+1}+\mathbf{R}^N\left(\mathbf{Y}^N_{n+1}\right)=\mathbf{L}^N\boldsymbol{\Lambda}_{n+1}+\mathbf{F}^N_{n+1}\\ \mathbf{M}^P\dot{\mathbf{Y}}^P_{n+\frac{j}{ss}}+\mathbf{R}^P\left(\mathbf{Y}^P_{n+\frac{j}{ss}}\right)=\mathbf{L}^P\boldsymbol{\Lambda}_{n+\frac{j}{ss}}+\mathbf{F}^P_{n+\frac{j}{ss}}\end{cases} \tag{3a}$$

$$\mathbf{G}^N\dot{\mathbf{Y}}^N_{n+1}+\mathbf{G}^P\dot{\mathbf{Y}}^P_{n+1}=\mathbf{0}, \tag{3b}$$

where **M**, **R**, and **F** are defined in 2 and signed Boolean collocation matrices **L** and **G** localize interface forces and define compatibility equations, respectively. The index n indicates the simulation time step while j loops from 1 to ss, which corresponds to the number of substeps performed by the integrator. Since the measured restoring force of the PS is inherently nonlinear, the corresponding state-space model does not include nonlinear evolution equations. A coarse time step Δt^N is used to solve the NS response whereas a time step Δt^P is used for computing the PS response. Two parameters define the setting of the PG-α algorithm:

- the testing time scale $\lambda=\Delta t^C/\Delta t^P=\Delta t^S/\Delta t^N$
- the subcycling parameter $ss=\Delta t^N/\Delta t^P=\Delta t^S/\Delta t^C$

where Δt^S defines the time window allocated to compute the NS response while Δt^C is the time step of the control system.

In principle, the accuracy of the transfer system, which is determined by the combined effects of actuator lag, control–structure interaction, and substructuring scheme, determines the minimum value for the testing time scale that produces acceptable simulation errors. In this regard, a concise list of studies can be found in previous works.[27–30] Similarly, the performance of the real-time computational platform determines the minimum value for the subcycling parameters. It is noteworthy that time steps Δt^N and Δt^P refer to simulation time, which is a virtual time axis defined by the time integration process. On the other side, Δt^S and Δt^C refer to the wall-clock time of the laboratory. In order to guarantee smooth displacement trajectories, a single PS displacement response step is computed within a controller time step Δt^C.

A two-stage approach is used to compute the solution of (3), which is obtained by the superposition of *free* and *link* partial solutions. The *free* solution is computed by discarding coupling conditions, whereas the *link* solution is computed by solving a linearized interface problem:

$$\mathbf{Y}^P_{n+1}=\mathbf{Y}^{P,free}_{n+1}+\mathbf{Y}^{P,link}_{n+1}=\mathbf{Y}^{P,free}_{n+1}+\mathbf{Q}^P\boldsymbol{\Lambda}_{n+1}, \tag{4a}$$

$$\mathbf{Y}^N_{n+1}=\mathbf{Y}^{N,free}_{n+1}+\mathbf{Y}^{N,link}_{n+1}=\mathbf{Y}^{N,free}_{n+1}+\mathbf{Q}^N\boldsymbol{\Lambda}_{n+1}, \tag{4b}$$

$$\boldsymbol{\Lambda}_{n+1}=-\mathbf{H}^{-1}\left(\mathbf{G}^N\dot{\mathbf{Y}}^{N,free}_{n+1}+\mathbf{G}^P\dot{\mathbf{Y}}^{P,free}_{n+1}\right). \tag{4c}$$

A detailed derivation of the Steklov–Poincaré operators **H**, $\mathbf{Q}^P$, and $\mathbf{Q}^N$ is reported in Abbiati et al.[21] Compared to monolithic time integration, a major advantage of partitioned time integration is the explicit calculation of

interconnecting forces $\mathbf{\Lambda}_{n+1}$, which can be supplied to a dynamic identification model of the PS for the purpose online parameter estimation. Such a feature is exploited to simplify the synchronization of simulation and model updating processes during HS. For the sake of clarity, the block diagram of Figure 1 provides a graphical representation of the procedure for solving an HS step from t_n to t_{n+1}, which comprises the solution of a single simulation step for the NS, the solution of *ss* simulation substeps for the PS, and the online estimation of the parameters of the identification model of the PS.

As can be appreciated from the block diagram of Figure 1, PS free solution, NS free solution, and online PS parameter estimation are parallel independent processes, which can be concurrently executed on different CPU cores. The link solution acts as a synchronization task, which is performed at the end of every coarse time step.

In order to be hard real-time compatible, online parameter estimation must rely on a predetermined number of evaluations of the dynamic identification model of the PS. Accordingly, the UKF was adopted in this case.[9] Based on the information contained in the last observation of the PS state $\mathbf{Y}^{P}_{n+1}$, the UKF updates the parameter vector $\boldsymbol{\theta}^{P,id}_{n}$ to yield $\boldsymbol{\theta}^{P,id}_{n+1}$. In order to accomplish this goal, the initial state-space equation of the PS model is augmented by an additional process equation. This additional fictitious equation facilitates time variations of unknown parameters so that by starting from an initial guess the UKF response converges into an unbiased estimate of the parameter vector:

$$\mathbf{Y}^{P,id}_{n+1} = \mathbf{f}^{Y}\left(\mathbf{Y}^{P,id}_{n}, \mathbf{F}^{P,id}_{n}, \mathbf{Q}^{P,id}\mathbf{\Lambda}_{n}; \boldsymbol{\theta}^{P,id}_{n}\right) + \mathbf{v}^{Y}_{n}, \tag{5a}$$

$$\boldsymbol{\theta}^{P,id}_{n+1} = \boldsymbol{\theta}^{P,id}_{n} + \mathbf{v}^{\theta}_{n}, \tag{5b}$$

where $\mathbf{f}^{Y}\left(\mathbf{Y}^{P,id}_{n}, \mathbf{F}^{P,id}_{n}, \mathbf{Q}^{P,id}\mathbf{\Lambda}_{n}; \boldsymbol{\theta}^{P,id}_{n}\right)$ integrates the response of the PS identification model from t_n to t_{n+1}. In the proposed framework, a state-space formulation is also adopted for the PS identification model, which includes the evolution equation $\mathbf{g}^{P,id}(\mathbf{u}^{P,id}, \mathbf{v}^{P,id}, \mathbf{s}^{P,id})$ of the nonlinear restoring force of the PS $\mathbf{r}^{P,id}(\mathbf{u}^{P,id}, \mathbf{v}^{P,id}, \mathbf{s}^{P,id})$.

The variation of the augmented state vector over time is facilitated via $\mathbf{v}^{Y}_{n}$ and $\mathbf{v}^{\theta}_{n}$ that are zero-mean uncorrelated Gaussian processes with covariance matrices $\mathbf{V}^{Y}$ and $\mathbf{V}^{\theta}$, respectively. For the sake of simplicity, 5a and 5b are grouped together to form the state evolution equation 6a, which together with the observation equation 6b define the standard setting of the UKF:

$$\mathbf{X}_{n+1} = \mathbf{f}(\mathbf{X}_{n}) + \mathbf{v}_{n}, \tag{6a}$$

$$\mathbf{Z}_{n+1} = \mathbf{H}\mathbf{X}_{n+1} + \mathbf{w}_{n+1}, \tag{6b}$$

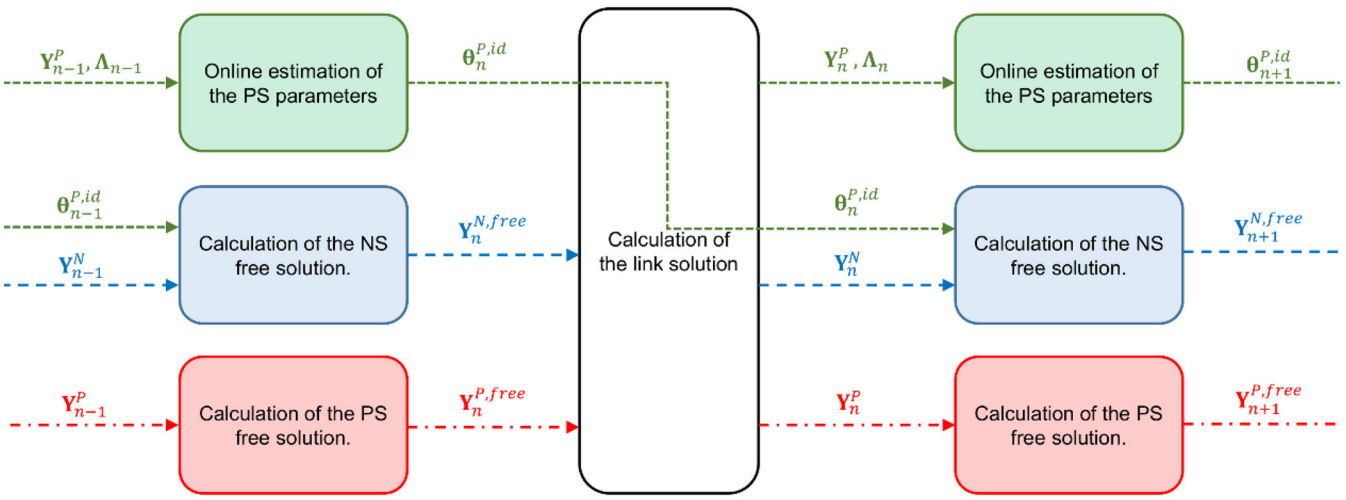

FIGURE 1 Block diagram of the procedure for solving an HS step from t_n to t_{n+1}

where $\mathbf{X}_n = \left[\mathbf{Y}_n^{P,id^T}\ \boldsymbol{\theta}_n^{P,id^T}\right]^T$ is the UKF augmented state of size L and $\mathbf{v}_n$ is a zero-mean uncorrelated Gaussian process with a covariance matrix:

$$\mathbf{V} = \begin{bmatrix} \mathbf{V}^Y & \mathbf{0} \\ \mathbf{0} & \mathbf{V}^\theta \end{bmatrix}. \tag{7}$$

Finally, the matrix $\mathbf{H}$ projects the only observable part of the augmented state to $\mathbf{Z}_{n+1}$. The latter is contaminated with a zero-mean uncorrelated Gaussian noise of covariance matrix $\mathbf{W}$, which represents measurement noise. In general, the observation equation 6b may take any form depending on the observed response quantities; however, for the sake of simplicity, here it is assumed that $\mathbf{H}$ is a Boolean matrix. The UKF procedure is summarized in the following.

1. Initialization of mean vector and covariance matrix of the filter state:

$$\hat{\mathbf{X}}_0 = \mathbb{E}[\mathbf{X}_0], \tag{8a}$$

$$\hat{\mathbf{P}}_0 = \mathbb{E}\left[\left(\mathbf{X}_0 - \hat{\mathbf{X}}_0\right)\left(\mathbf{X}_0 - \hat{\mathbf{X}}_0\right)^T\right]. \tag{8b}$$

2. Start the loop of n from 1 to N, which is synchronized to the time integration of the NS response as described in Figure 1.
3. Generation of $2L+1$ samples of the state vector, which corresponds to the so-called sigma points:

$$\boldsymbol{\chi}_{n,l}^- = \begin{cases} \hat{\mathbf{X}}_n & l = 2L+1 \\ \hat{\mathbf{X}}_n + \left(\sqrt{(L+\kappa)\left[\hat{\mathbf{P}}_n\right]}\right)_l & 1 \le l \le L \\ \hat{\mathbf{X}}_n - \left(\sqrt{(L+\kappa)\left[\hat{\mathbf{P}}_n\right]}\right)_{l-L} & L+1 \le l \le 2L \end{cases}, \tag{9}$$

where subscript l indicates the l-th column of the matrix $\sqrt{(L+\kappa)\left[\hat{\mathbf{P}}_n\right]}$, while parameter κ provides an extra degree of freedom to fine-tune the estimation of the higher-order moments of the state approximation providing that $(L+\kappa) \neq 0$. In case the distribution of the state vector is assumed to be Gaussian, it is suggested using $L+\kappa = 3$.[9]

$$\boldsymbol{\chi}_{n+1,l}^- = \mathbf{f}\left(\boldsymbol{\chi}_{n,l}\right). \tag{10}$$

Prediction of the augmented state statistics based on sigma-point samples:

$$\hat{\mathbf{X}}_{n+1}^- = \sum_{l=1}^{2L+1} \omega_l \boldsymbol{\chi}_{n+1,l}^-, \tag{11a}$$

$$\hat{\mathbf{R}}_{n+1}^- = \sum_{l=1}^{2L+1} \omega_l \left(\boldsymbol{\chi}_{n+1,l}^- - \hat{\mathbf{X}}_{n+1}^-\right)\left(\boldsymbol{\chi}_{n+1,l}^- - \hat{\mathbf{X}}_{n+1}^-\right)^T, \tag{11b}$$

$$\hat{\mathbf{P}}_{n+1}^- = \hat{\mathbf{R}}_{n+1}^- + \mathbf{V}, \tag{11c}$$

where the weighting factors ω_l are calculated as

$$\omega_l = \begin{cases} \dfrac{\kappa}{L+\kappa} & l = 2L+1 \\ \dfrac{1}{2(L+\kappa)} & l \neq 2L+1 \end{cases}. \tag{12}$$

Calculation of Kalman gain:

$$\mathbf{K}_{n+1} = \hat{\mathbf{P}}_{n+1}^{-}\mathbf{H}^T\left(\mathbf{H}\hat{\mathbf{P}}_{n+1}^{-}\mathbf{H}^T + \mathbf{W}\right)^{-1}. \tag{13}$$

Update of augmented state statistics based on last measurements:

$$\hat{\mathbf{X}}_{n+1} = \hat{\mathbf{X}}_{n}^{-} + \mathbf{K}_{n+1}\left(\mathbf{Z}_{n+1} - \mathbf{H}\hat{\mathbf{X}}_{n+1}^{-}\right), \tag{14a}$$

$$\hat{\mathbf{P}}_{n+1} = \hat{\mathbf{P}}_{n+1}^{-} - \mathbf{K}_{n+1}\mathbf{H}\hat{\mathbf{P}}_{n+1}^{-}. \tag{14b}$$

If $n < N$ stop the procedure, otherwise set $n = n+1$ and go to Step 3.

The covariance matrices $\mathbf{V}$ and $\mathbf{W}$ are proportional to model and measurement errors, respectively. To ensure a stable state estimate, they are tuned before the HS based on numerical simulations that account for both measurement noise and model error between the PS and the corresponding identification model. A more comprehensive discussion on stability and accuracy issues related to the setting of the UKF within the scope of HS with online model updating is presented in Ou et al.[31]

2.2 | Experimental implementation at EUCENTRE

The HS framework described in Section 2.1 was implemented at the Experimental Laboratory of EUCENTRE, Pavia, Italy.[32] In this regard, the block diagram of Figure 2 provides an overview of the architecture of the implementation.

As can be appreciated from Figure 2, a Windows-based PC was used to assemble and compile the SIMULINK model of the HS framework, which was then downloaded into the xPC Target and executed in hard real-time mode. In line with the block diagram of Figure 1, NS free solution, PS free solution, and online estimation of PS parameters were implemented as three separate referenced models configured for concurrent execution using three different CPU cores. For a detailed description of concurrent execution of referenced models, the reader is addressed to the MATLAB/SIMULINK manual.[18] The simulation step of the xPC Target was set to 1/1,024 s, that is, the same time step size Δt^C of both MTS FLEXTEST and Bearing Testing System (BTS) controllers. A fixed time step size Δt^N of 1/1,024 s was set for solving the NS free response and thus the online estimation of PS parameters. Accordingly, the value of the subcycling parameter *ss* was always set equal to the testing time scale λ.

3 | VIRTUAL BRIDGE PROTOTYPE

3.1 | Description of the case study

A virtual two-pier prototype bridge was selected to validate the proposed framework. Such a bridge is characterized by a three-span RC deck with two independent roadways sustained by two twin cantilever RC piers with rectangular hollow cross-sections. Besides supporting the verification of the proposed framework, the purpose of the experimental campaign was to assess the performance of a realistic RC bridge with inadequate seismic steel reinforcement detailing in both as-built and isolated configurations. Figure 3 depicts the corresponding AB and ISO configurations investigated via HS. Figure 4 reports the cross-sections of the deck and the pier, while Table 1 summarizes the related geometrical properties.

Figure 5 depicts deck-to-pier connections for both AB and ISO configurations, including pier reinforcement detailing. As can be appreciated, the longitudinal reinforcement of each pier comprised two grids of ϕ20 rebars with 200 mm

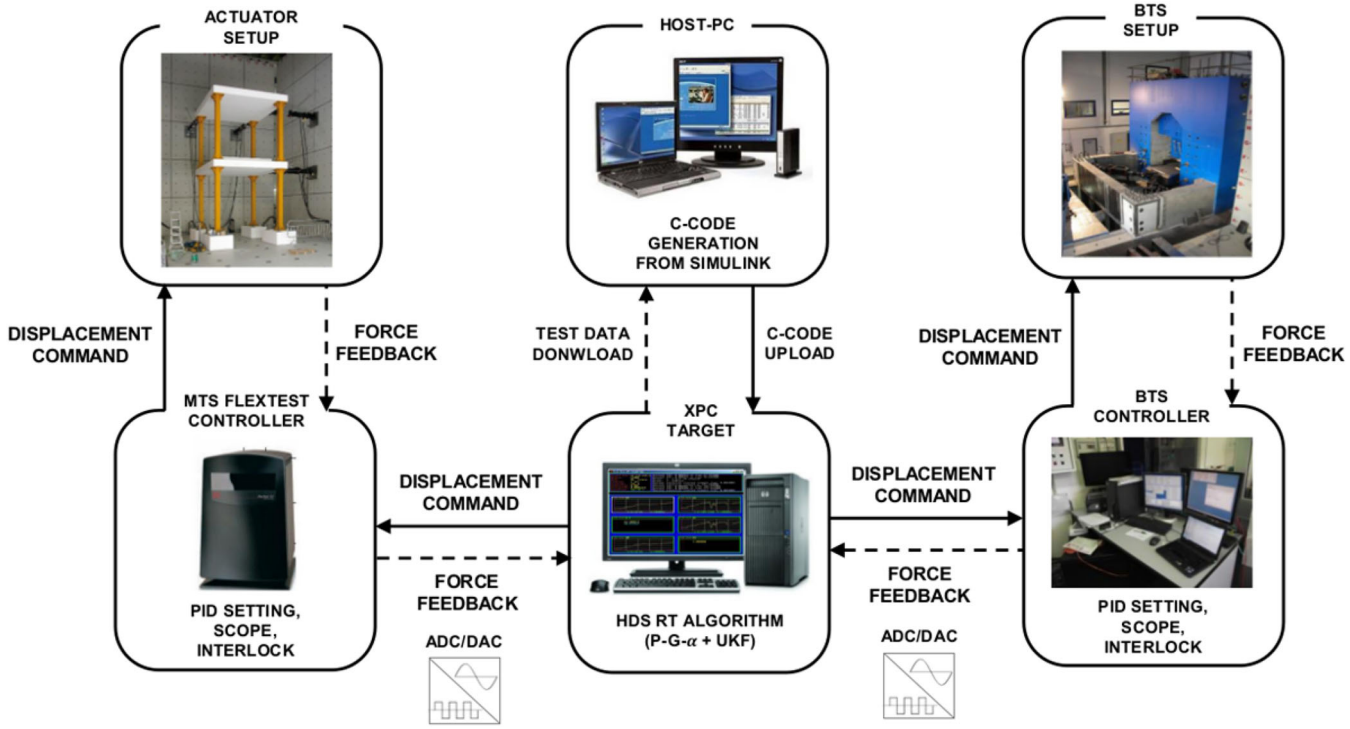

FIGURE 2 Architecture of the implementation of the HS framework at the Experimental Laboratory of EUCENTRE, Pavia, Italy: the MTS FLEXTEST controller is used for the actuator setup while the Bearing Testing System (BTS) is provided with a proprietary controller. Both controllers are interfaced with the xPC Target, which coordinates the HS

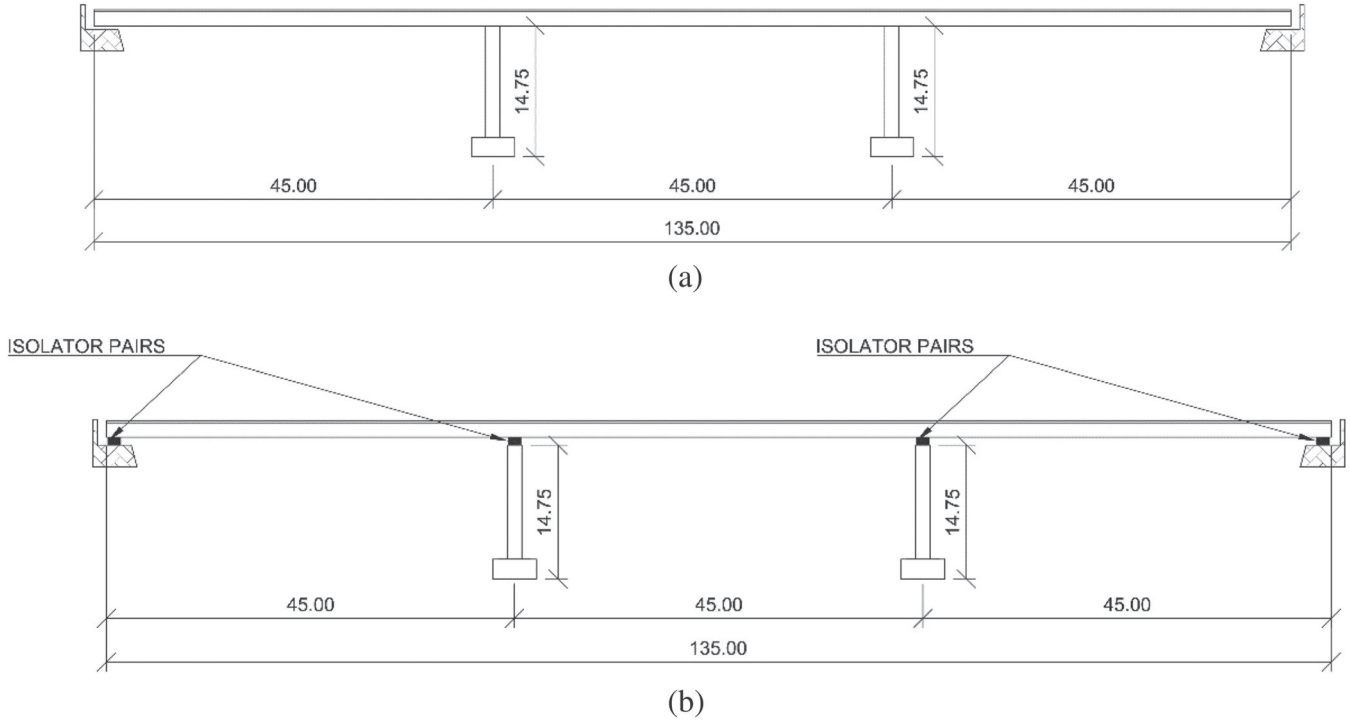

FIGURE 3 Virtual bridge prototype with main dimensions in meters: (a) AB and (b) ISO configurations

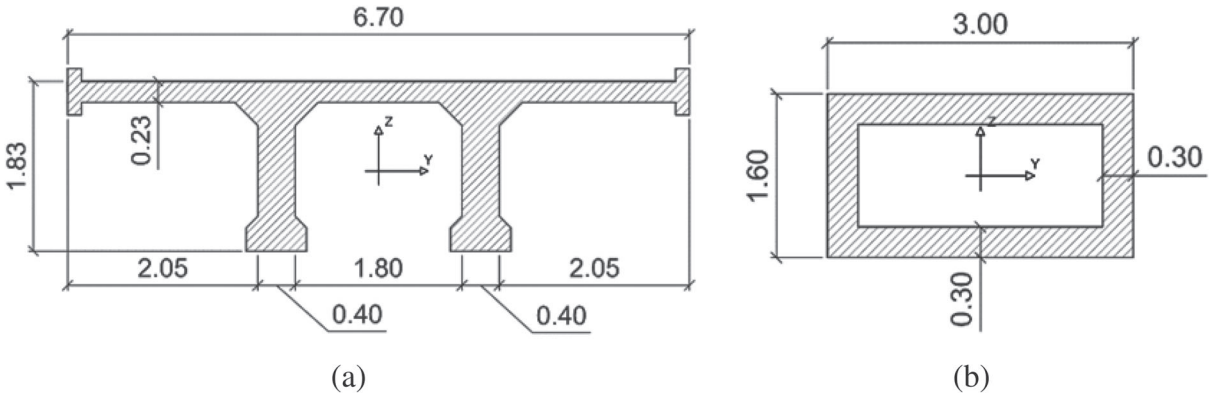

FIGURE 4 Cross-sections of (a) deck and (b) pier

TABLE 1 Geometrical properties of cross-sections

Property	Deck	Pier
A	2.78 m^2	2.40 m^2
I_{zz}	7.20 m^4	0.82 m^4
I_{yy}	0.85 m^4	2.40 m^4

spacing POS.#2- and POS.#3-. On the other side, ϕ12 stirrups with 200 mm spacing (POS.#1) characterized the transversal reinforcement.

As depicted in Figure 5b, a pair of double-curvature concave sliding bearings (D-CSBs) was interposed between the deck and each pier in the configuration ISO. An additional pair of D-CSBs was interposed between the deck and each abutment in this case. D-CSBs were dimensioned to limit the lateral force applied to each pier to 370 kN, which corresponds to a lateral displacement of 10 mm in full-scale. The total vertical load applied to each pier was equal to 4,000 kN. Section 3.3 provides a detailed description of the tested D-CSB, including main dimensions and parameters.

3.2 | Finite-element modeling and ground motion selection

In order to support the design of the HS campaign, a reference FE model of the bridge was implemented using the OpenSees FE software.[33] Linear beam elements were used for the deck, while fiber-based nonlinear beam elements were used for piers. Figure 6 depicts a schematic of the OpenSees FE model with node numbering and constraint conditions.

The seismic acceleration was oriented along the y axis. The rigid links accounted for the offset between pier cap beams and deck center of gravity, as depicted in Figure 7. In addition, relative y and z rotations between the deck and rigid links were released. Numerical simulations performed with the OpenSees FE model showed that the release of both y and z relative rotations does not affect the lateral response of the bridge to seismic loading. However, it strongly simplifies the experimental substructuring of the physical pier, which was tested under in-plane loading conditions, as explained in Section 3.3.1.

The *Concrete02* material was used for concrete, while the *Steel02* material was used for rebars of fiber-based cross-sections. Figure 8 depicts the stress–strain relationship of both material models, together with relevant parameters.

Parameter values were calibrated based on the results of previous quasi-static cyclic tests performed on a 1:2 scale mock-up specimen of the pier.[34] Table 2 reports the first five vibration periods of the bridge in the configuration AB predicted by the OpenSees FE model.

A 5% proportional Rayleigh damping was tuned on Modes #1 and #5, which were characterized by the two highest modal participation factors in the direction of the seismic loading. Such a value is meaningful for concrete structures excited close to yield and thus exhibiting considerable cracking.[35]

The REXEL software[36] was used to select a single ground motion record corresponding to a seismic scenario characterized by moment magnitude $M = 5$–7, epicentral distance $D = 0$–30 km, and soil type B. Target values of peak ground

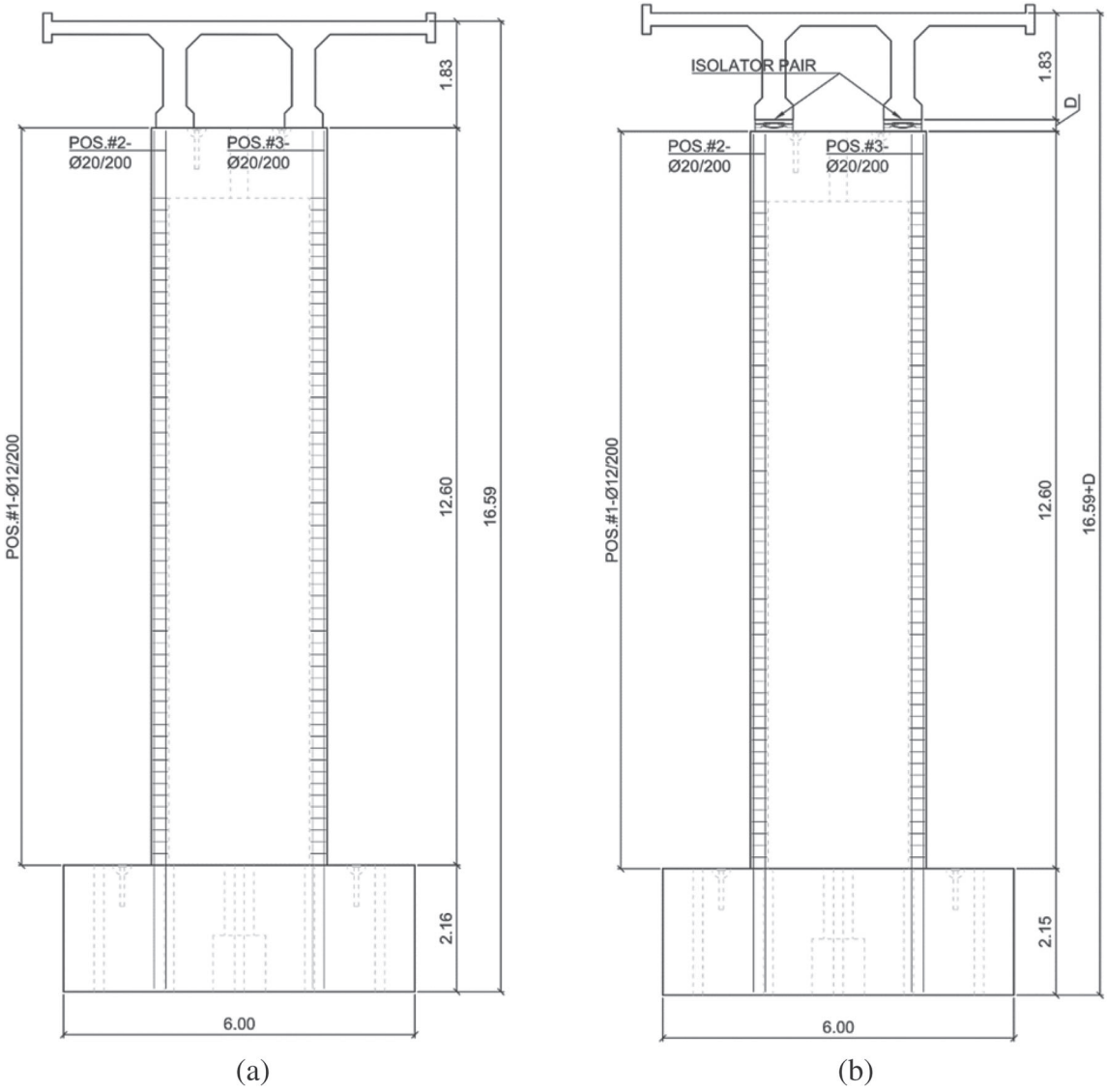

FIGURE 5 Deck-to-pier connection: (a) AB; (b) ISO configurations

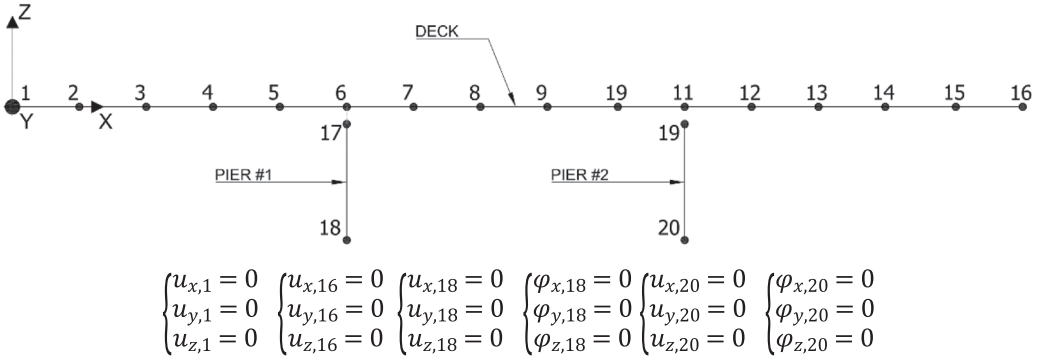

FIGURE 6 OpenSees FE model of the virtual prototype bridge

acceleration (PGA) for scaling the accelerogram were identified by means of time history response analyses of the OpenSees FE model in the configuration AB. In detail, a PGA = 0.12 g was assigned to the Serviceability Limit State (SLS), while a PGA value of 0.30 g was selected for the Ultimate Limit State (ULS). In this regard, Figure 9 depicts both

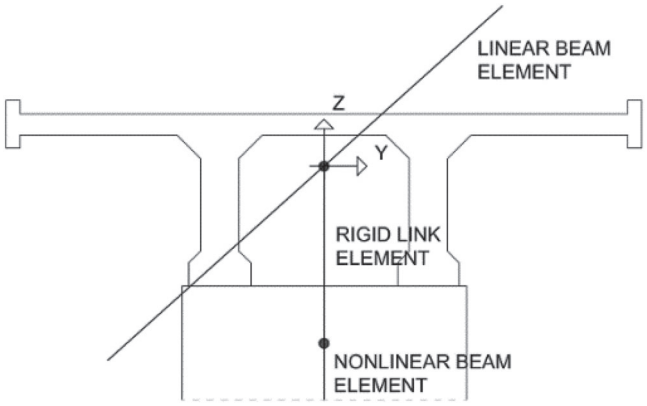

FIGURE 7 Deck-to-pier connection based on rigid link elements

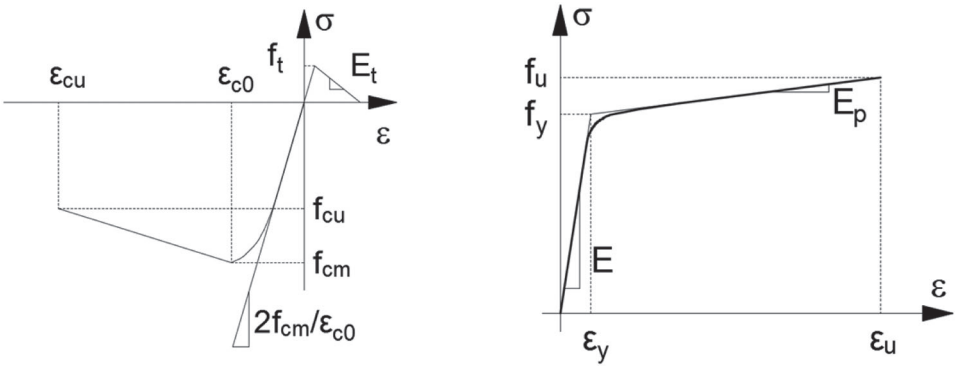

$f_{cm} = 55$ MPa, $f_{cu} = 44$ MPa, $f_t = 5.5$ MPa
$\varepsilon_{c0} = 0.40$ %, $\varepsilon_{cu} = 0.60$ %
(a)

$f_y = 525$ MPa, $E = 200$ GPa
$E_p/E = 0.015$
(b)

FIGURE 8 Backbone curves of stress–strain relationships: (a) *Concrete02*; (b) *Steel02* OpenSees materials adopted for RC members

TABLE 2 Vibration periods of the virtual prototype bridge in the configuration AB

Mode	Period (s)
#1	0.639
#2	0.500
#3	0.392
#4	0.344
#5	0.320

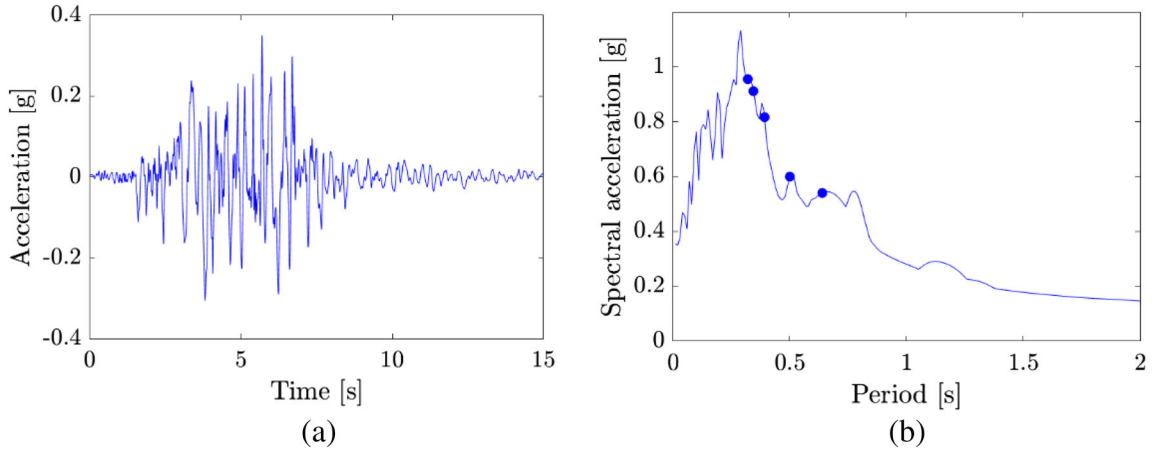

FIGURE 9 Selected seismic ground motion scaled to PGA = 0.30 g for the ULS: (a) accelerogram; (b) acceleration response spectrum for equivalent viscous damping of 5%

the accelerogram and the relevant elastic acceleration response spectrum for the ULS case; black dots highlight bridge periods reported in Table 2.

The effectiveness of the seismic isolation schemes was preliminary verified via OpenSees FE simulations. In this regard, Figure 10 compares the hysteretic loops of the transversal restoring force on Pier #1 in the configurations AB and ISO after SLS and ULS time history analyses.

As can be appreciated in Figure 10, OpenSees simulations predicted a linear response for Pier #1 during the SLS earthquake. A remarkable hysteresis was predicted instead during the ULS in the configuration AB. A linear response was predicted for both SLS and ULS records in the ISO configuration.

3.3 | Experimental dynamic substructuring

Figure 11 depicts the substructuring schemes of the hybrid models of the bridge for both AB and ISO configurations.

According to Figure 11, both substructuring schemes combine different sets of PSs and NSs, which are depicted in red and blue, respectively. Nonlinear springs represent nonlinear substructures, that is, RC piers and seismic isolators, which can be either physical or numerical. More precisely, in the configuration AB, the 1:2 scale mock-up of the RC pier was tested with servo-hydraulic actuators while the remaining substructures were simulated numerically. Both the 1:2 scale mock-up of the RC pier and one of the two corresponding isolation devices were tested in the laboratory in the ISO. A single bearing per pair was physically tested, and the measured restoring force feedback was multiplied by two. This latter simplification was preliminary verified with numerical simulations, which proved that the deck overturning moment was negligible and did not affect the transversal response of the bridge. Although a 1:2 scale mock-up of the RC pier was tested in the laboratory, hybrid models were at full-scale. To this end, actuator displacements and corresponding forces were adequately scaled. Finally, the deck super-element was obtained via static condensation of the linear deck of the OpenSees FE model, by retaining transversal displacements of Nodes #6 and #11 for configuration AB and Nodes #1, #6, #11, and #16 for configurations ISO, respectively (see Figures 6 and 11 for node numbering).

A 5% proportional Rayleigh damping was tuned on Modes #1 and #5, of the linearized version of the hybrid model of the bridge in the AB configuration and used for all experiments. As suggested by Molina and co-workers,[37] HSs were performed without adding numerical viscous damping to the PSs, whose restoring forces already incorporate dissipative components.

3.3.1 | Substructuring of the RC concrete pier

The hybrid model of the virtual bridge prototype combined two identical piers and eight identical D-CSBs, but only some of these were tested in the laboratory. Therefore, state-space models were derived and calibrated for each PS. Figure 12 reports a schematic of the test setup of the 1:2 scale mock-up of the RC pier with main dimensions and a picture of the laboratory installation.

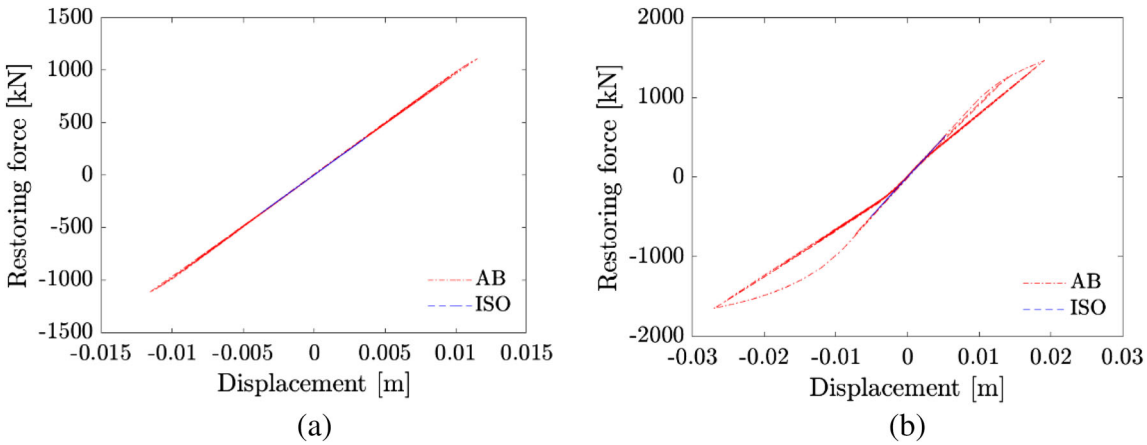

FIGURE 10 Hysteretic loop of the transversal restoring force of Pier #1 predicted by the OpenSees FE model: (a) PGA of 0.12 g for the SLS; (b) PGA of 0.30 g for the ULS

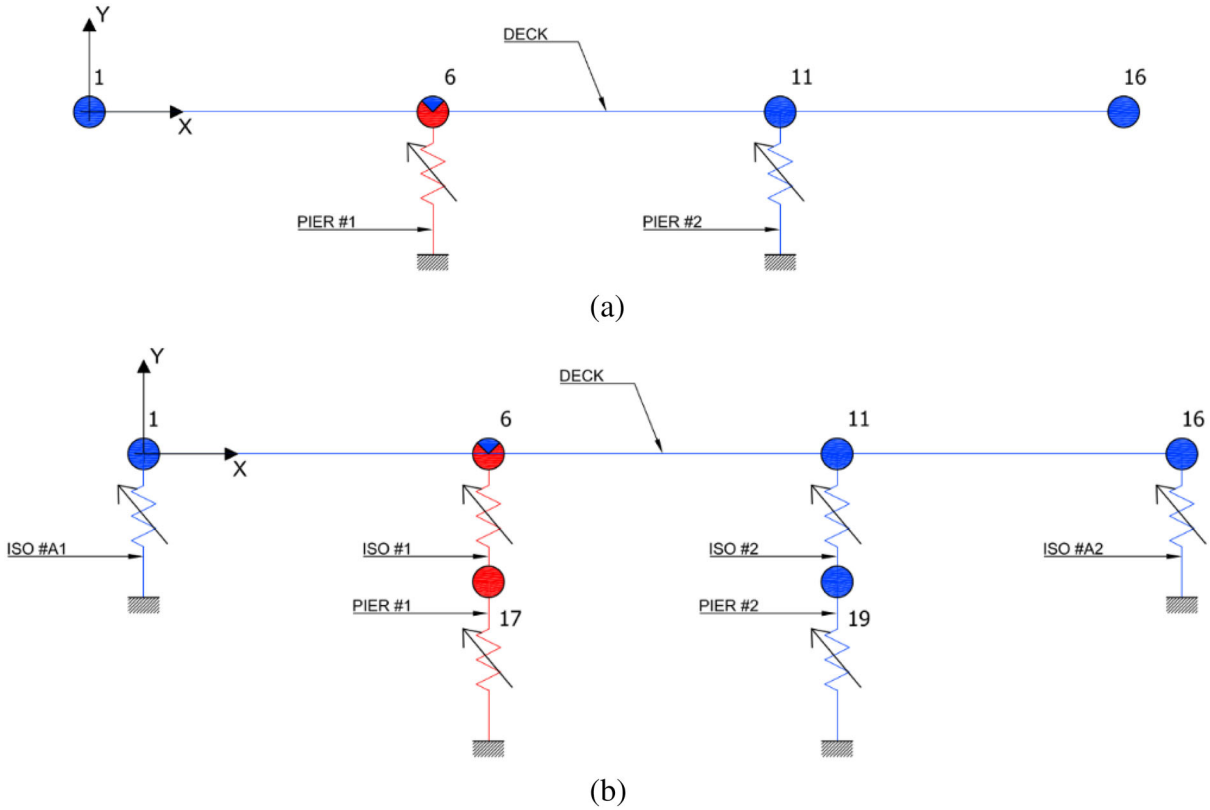

FIGURE 11 Plan views of the substructured virtual bridge prototype: (a) AB; (b) ISO configurations

As can be appreciated from Figure 12a, 14Ø42 post-tensioned steel bars fully restrained the RC pier mock-up at the base. One horizontal actuator with 1,000 kN force capacity was connected at the cap level using a post-tensioned loading system made of two 0.150 m thick steel plates embracing the pier along the direction of motion. However, the flexibility of the post-tensioned loading system was not negligible compared to the pier. Therefore, a piecewise linear spring was calibrated and used to adjust the actuator command:

$$d_{cmd} = d_{des} + \frac{r_{fbk}}{k}, \tag{15a}$$

$$k = \begin{cases} 1{,}650\,\text{kN/m}, r_{fbk} \geq 0 \\ 2{,}500\,\text{kN/m}, r_{fbk} < 0 \end{cases}, \tag{15b}$$

where d_{des} stands for the desired displacement to be applied to the pier, while d_{cmd} is the compensated actuator command. On the other side, r_{fbk} is the force feedback measured from the actuator load cell, and k is the piecewise linear stiffness of the post-tensioned loading system. The verification of such compensation procedure was performed by comparing the desired displacement command to an external LVDT measurement, which was not affected by the deformability of the actuator connection. In this respect, Figure 13 compares the target and actual pier transversal displacements to the corresponding actuator command for a generic verification test.

As can be appreciated from Figure 13, the implemented compensation strategy almost eliminated control errors. As a result, it was possible to exclude external transducers from the control loop. A hollow hydraulic jack with 2,000 kN force capacity imposed the nominal vertical load to the pier by pulling a high strength Ø64 steel bar anchored to the reaction floor. Besides, as depicted in Figure 14, 29 LVDTs monitor the local pier behavior on both sides.

A nonlinear S-DoF state-space model was constructed to simulate the response of the numerical pier. In detail, mass, stiffness, and seismic inertia of the S-DoF state-space model were obtained by static condensation of the FE matrices of the pier constructed in OpenSees. In this case, only the transversal displacement at the cap level of the pier was retained as master DoF. All remaining DoFs were discarded. In order to approximate the hysteretic behavior of the

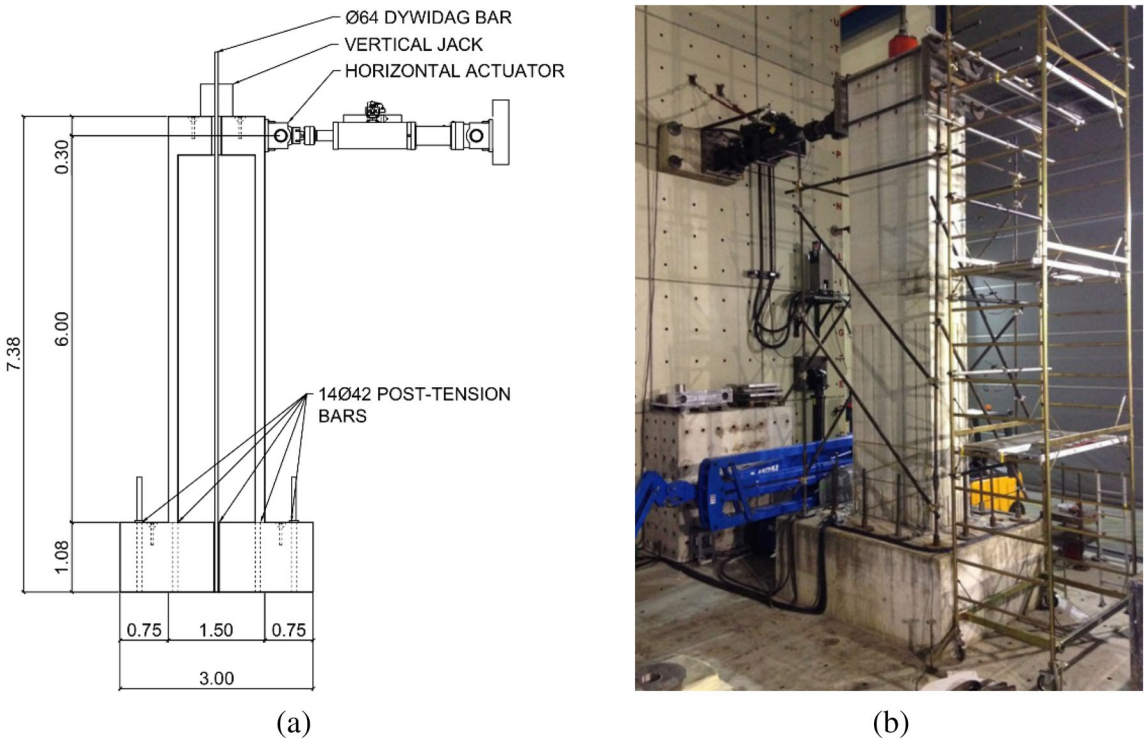

FIGURE 12 Test setup of the 1:2 scale mock-up RC pier: (a) schematic of the loading system (dimensions in meters); (b) installation at the Experimental Laboratory of EUCENTRE, Pavia, Italy

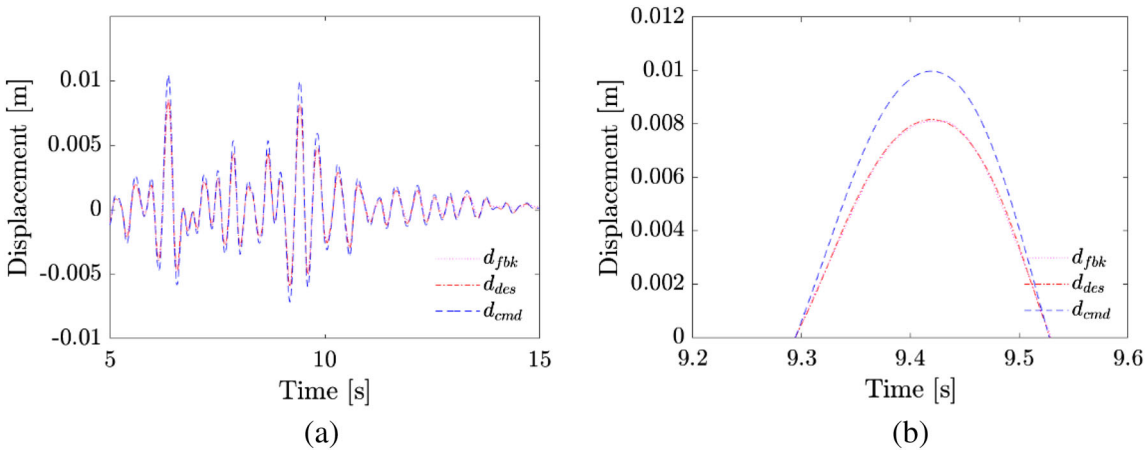

FIGURE 13 Compensation of the deformability of the horizontal loading system of the pier: (a) entire time history; (b) close-up view of a single oscillation peak

OpenSees pier, a nonlinear Bouc-Wen spring was calibrated based on the OpenSees simulation at ULS, where a nonlinear hysteretic response was observed:

$$\begin{cases} \dot{r} = (A_{BW} - (\beta_{BW}\,\mathrm{sign}(vr) + \gamma_{BW})|r|^{n_{BW}})v \\ \dot{u} = v \end{cases}, \tag{16}$$

where u, v, and r are displacement, velocity, and restoring force of the Bouc-Wen spring; moreover, A_{BW} was set equal to the S-DoF stiffness of the condensed FE model of the pier, and $\beta_{BW} = 3.5$, $\gamma_{BW} = 60$, and $n_{BW} = 1$ are the calibrated nonlinear parameters. In detail, nonlinear static analysis of the reduced nonlinear S-DoF spring described by 16 was

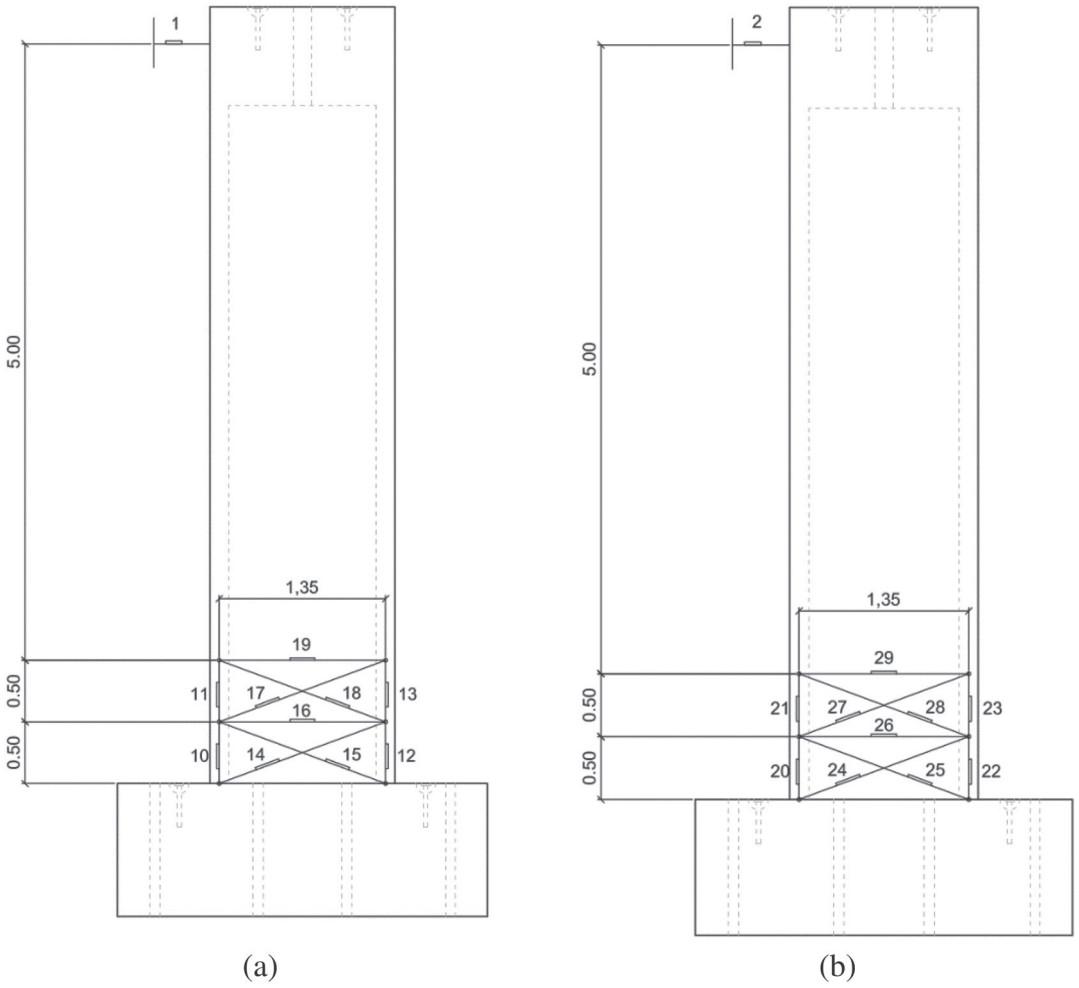

FIGURE 14 Positioning of LVDT sensors on the 1:2 scale mock-up RC pier: (a) front and (b) back views (dimensions in meters)

performed by imposing the displacement response history obtained from the OpenSees simulation at the ULS; and parameters were calibrated to match the corresponding force response. In this respect, Figure 15 compares the OpenSees and the nonlinear S-DoF Bouc-Wen spring responses.

3.3.2 | Substructuring of seismic isolation devices

The BTS of the Experimental Laboratory of EUCENTRE was designed to test full-scale seismic isolation devices.[32] In detail, the specimen is positioned on a self-equilibrating vertical reaction structure; the bottom plate of the specimen is connected to a 6-DoF shake table, driven by vertical and horizontal actuators and connected to an additional horizontal reaction structure, which can be operated in mixed force-displacement control. The maximum vertical and horizontal load capacities of the BTS are 50 and 2.8 MN, respectively. The allowed horizontal displacement range is $\pm$0.495 m, with a velocity peak of 2.2 m/s. In order to eliminate spurious friction and inertia components, eight ring prestressed load cells measure both components of the horizontal restoring force of the tested isolation device directly from its support plate, which slides on a Teflon sheet. In this regard, Figure 16 shows the BTS setup and provides a close-up view of the restoring force measuring system.

It is noteworthy that the interaction between displacement controlled actuators and stiff specimens easily triggers dynamic instability. This situation is very likely to occur on elements subjected to axial deformation, where small perturbations generate large feedback forces. In order to overcome this problem, the common practice consists of excluding vertical DoFs from the HS loop and impose nominal loads in force control. Accordingly, the nominal vertical load

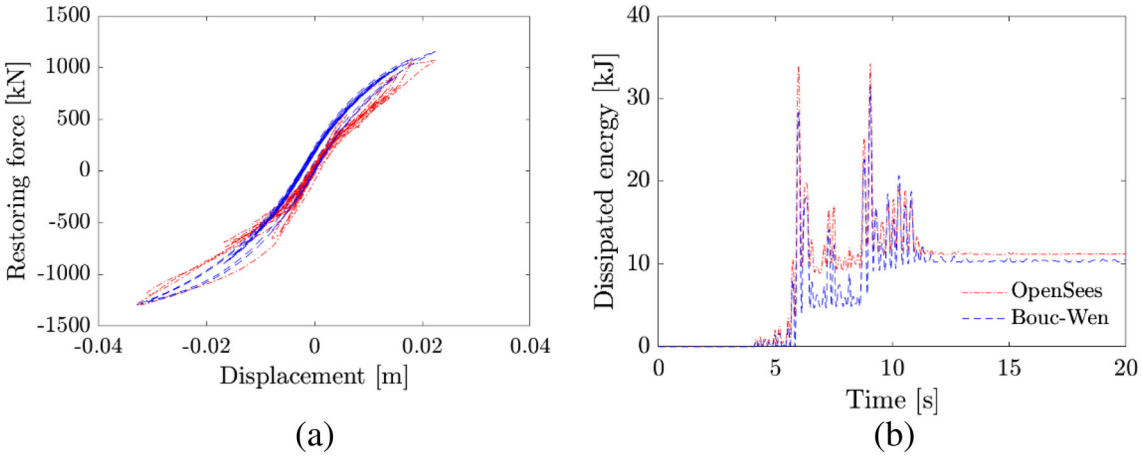

FIGURE 15 Validation of the nonlinear S-DoF reduced RC pier against OpenSees: (a) hysteretic loop of the transversal shear force; (b) corresponding cumulative dissipated energy history

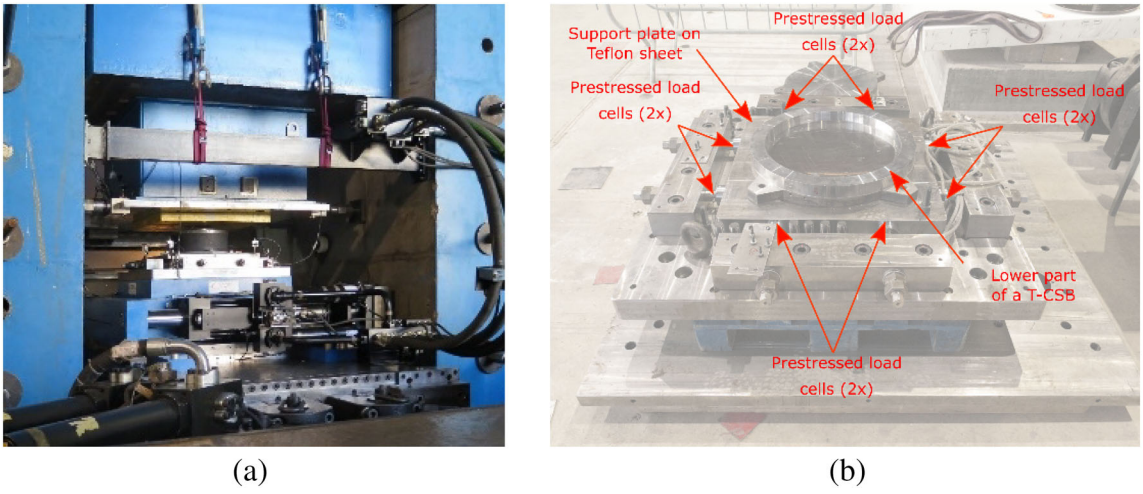

FIGURE 16 Bearing Testing System: (a) test setup with a seismic isolation device installed; (b) force measuring system based on prestressed load cells

owing to the self-weight of the bridge deck was kept constant and applied to the tested seismic isolation device in force control, while displacement control was used for the horizontal DoF only, which was included in the HS loop.

The selected D-CSB device designed by EUCENTRE[38,39] was characterized by two sliding surfaces with equivalent radius $R = 3.08$ m and coated with graded polytetrafluoroethylene (PTFE) filled with carbon fiber, displacement capacity of ± 0.25 m in all directions, and maximum allowed vertical load of 3,100 kN. Figure 17 reports a schematic of a generic D-CSB,[40] with the main characteristics highlighted.

The differential model proposed by Mostaghel[26] was adopted to emulate numerical D-CSBs during HS. Figure 18 provides an overview of the Mostaghel model.

The corresponding ODE set, which defines the relevant hysteretic restoring force, reads

$$\begin{cases} \dot{r} = (\alpha_{MST} k_{MST} + (1-\alpha_{MST}) k_{MST} (\bar{N}(v)\bar{M}(s-\delta_{MST}) + M(v)N(s+\delta_{MST})))v \\ \dot{u} = v \end{cases}, \tag{17}$$

with

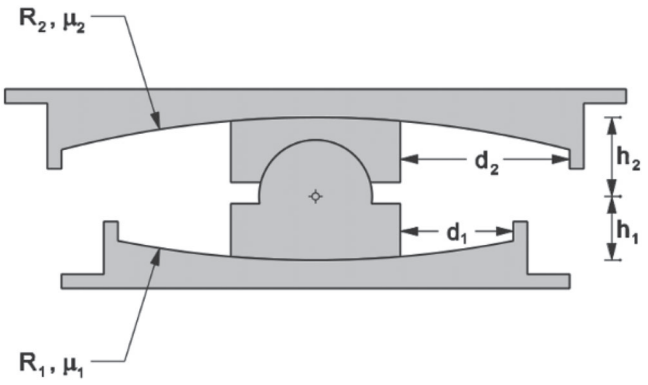

FIGURE 17 Schematic of a D-CSB device after Fenz and Constantinou[40]

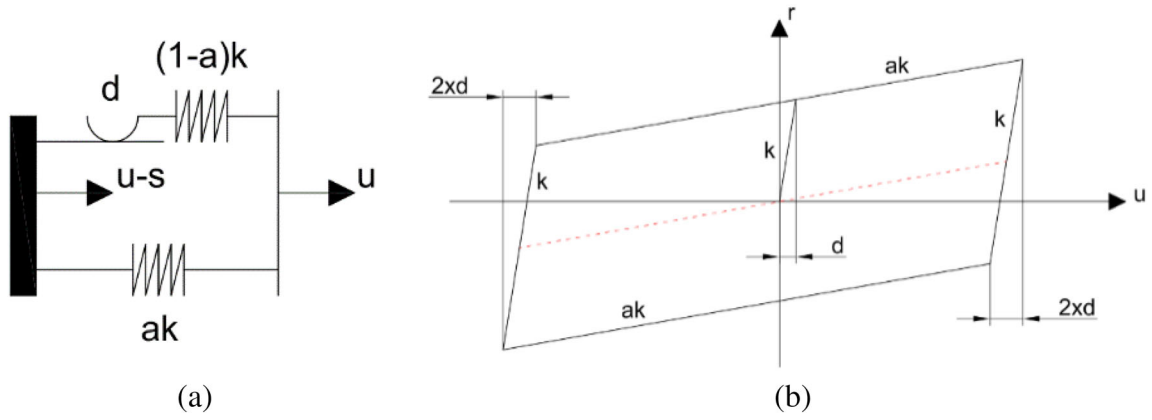

FIGURE 18 Mostaghel's bilinear elastoplastic spring: (a) spring-slider idealization; (b) hysteretic loop

$$s = \frac{r - \alpha_{MST} k_{MST} u}{(1 - \alpha_{MST}) k_{MST}}, \tag{18}$$

where u, v, and r represent displacement, velocity, and restoring force state variables while s is the slip displacement. Model parameters k_{MST}, α_{MST}, and δ_{MST} define initial stiffness, post-yield stiffness reduction, and yield displacement, respectively. Values identified for the maximum velocity peak of 0.20 m/s, which corresponds to sliding friction $\mu = 8\%$, read

$$k_{MST} = 166{,}000\,\text{kN/m}, \quad \alpha_{MST} = 0.0035, \; \delta_{MST} = 0.001\,\text{m}.$$

The remaining functions N, M, $\bar{N}$, and $\bar{M}$ are defined as follows:

$$\begin{aligned} N(w) &= 0.5(1 + \text{sgn}(w))(1 + (1 - \text{sgn}(w))) \\ M(w) &= 1 - N(w) \\ \bar{N}(w) &= M(-w) \\ \bar{M}(w) &= N(-w). \end{aligned} \tag{19}$$

Figure 19 compares the response of the D-CSB during the cyclic characterization test with a velocity peak of 0.2 m/s to the response predicted by the Mostaghel's model.

In order to compensate for the rate dependency of the friction coefficient of the sliding surfaces of the CSB, a vertical load correction was applied as analogously done in Bursi et al.[20]

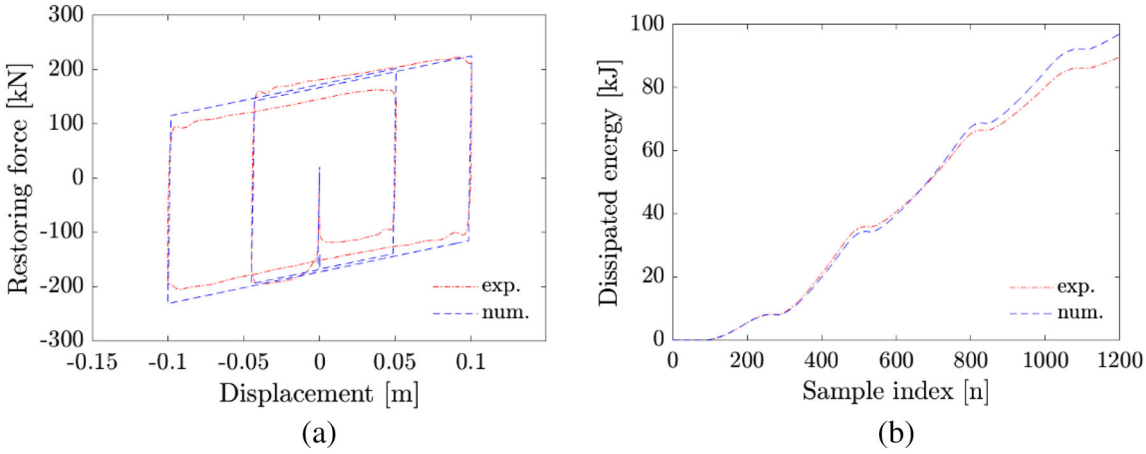

FIGURE 19 Validation of the D-CSB model against experimental measurements at $v = 0.2$ m/s: (a) hysteretic loop; (b) dissipated energy history

4 | RESULTS OF HYBRID SIMULATIONS

The HS campaign HT3 started in February 2015 and included both Pier #1 and one D-CSB device as PSs. The response of the virtual bridge prototype was evaluated for configuration AB and ISO. Table 3 summarizes the list of tests carried out and relevant information. In order to induce slight damage to the physical Pier #1, three tests were carried out in the configuration AB up to 0.50 g of PGA. Isolated tests were conducted afterward up to 0.75 g of PGA. Successively, HSs of the AB response were performed up to 0.85 g of PGA, where a significant hysteretic response of the tested pier was observed.

As can be appreciated from Table 3, all experiments were conducted in the pseudodynamic regime because of the limited actuation capacity of the pier setup. However, the hard real-time implementation of the presented HS framework is suitable for fast- and real-time HS, as demonstrated in Abbiati et al.[21] For the sake of comparison, all reported plots refer to the virtual bridge prototype at full-scale. Accordingly, PS displacement and restoring force histories are multiplied by 2 and 4, respectively.

4.1 | Results for the as-built configuration

HSs in the configuration AB were conducted by scaling the selected accelerogram up to 0.85 g of PGA. In this regard, Figure 20 reports the hysteretic response of Pier #1 measured during four different tests; in addition, Figure 21 shows the crack pattern at the pier base at the end of the testing campaign.

From Figure 20, one can deduce that PGA values up to 0.50 g did not produce remarkable hysteresis. However, the OpenSees FE model predicted a PGA value of 0.30 g for triggering ULS damage. Such bias can be ascribed to base rocking, which was not accounted for in the numerical simulation.

TABLE 3 Program of the HT3 testing campaign

Test	Date	Configuration	PGA (g)	PS	Online updating	Time scale λ
HT3-52	05/02/2015	AB	0.35	PIER	Yes	128
HT3-55	06/02/2015	ISO	0.35	PIER, D-CSB	No	256
HT3-57	06/02/2015	ISO	0.50	PIER, D-CSB	No	256
HT3-58	06/02/2015	ISO	0.75	PIER, D-CSB	No	256
HT3-60	09/02/2015	AB	0.50	PIER	Yes	128
HT3-65	10/02/2015	AB	0.75	PIER	No	128
HT3-70	11/02/2015	AB	0.85	PIER	No	256

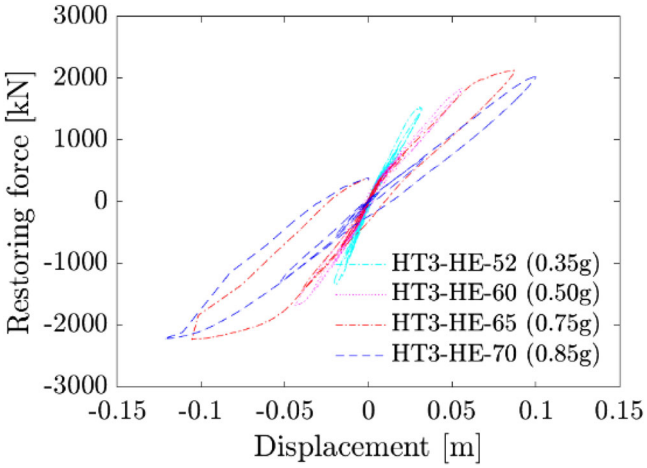

FIGURE 20 Hysteretic loops of the restoring force of the physical pier

FIGURE 21 Crack pattern at the base of the physical pier after Test HE-70

The UKF was used to estimate the parameters of the identification model of Pier #1 (PS) online and then used to update the parameters of Pier #2 (NS). Specifically, the same S-DoF system endowed with the Bouc-Wen restoring force model of 16 was used both as identification model of Pier #1 and computational model of Pier #2.

Preliminary numerical simulations based on synthetic noise-contaminated response signals obtained with the OpenSees FE model produced unstable estimates when the UKF parameter estimation process included the entire set of parameters of the Bouc-Wen model defined in 16. This issue can be reasonably ascribed to the naïve functional form of the dynamic identification model. Therefore, during HS, the UKF estimation was limited to the elastic tangent stiffness parameter A_{BW}, whose initial value was calibrated on the low-amplitude cyclic response of the physical pier.

Figure 22a compares the hysteretic loop of the restoring force of Pier #1, which was tested in the laboratory, and Pier #2, simulated by the Bouc-Wen spring updated online. Along the same line, Figure 22b reports the time history of the estimate of the parameter A_{BW} provided by the UKF. In this case, the UKF was able to track the stiffness degradation of Pier #1. However, for PGA values greater than 0.50 g, the tangent stiffness estimate was not stable. Therefore, the online model updating of Pier #2 was disabled.

4.2 | Results for the isolated configuration

Figure 23 compares the hysteretic loops of the restoring force measured on the physical pier in configurations AB and ISO. The effectiveness of the isolation system based on D-CSBs on the pier response is evident.

As depicted in Figure 23, the seismic isolation system based on D-CSBs limits the maximum transversal displacement experienced by the physical pier within the range ±10 mm (full-scale). On the other hand, Figure 24 compares the force-displacement responses of the tested D-CSB for two PGA levels. In both cases, the maximum shear force transferred to the physical Pier #1 remained below 200 kN.

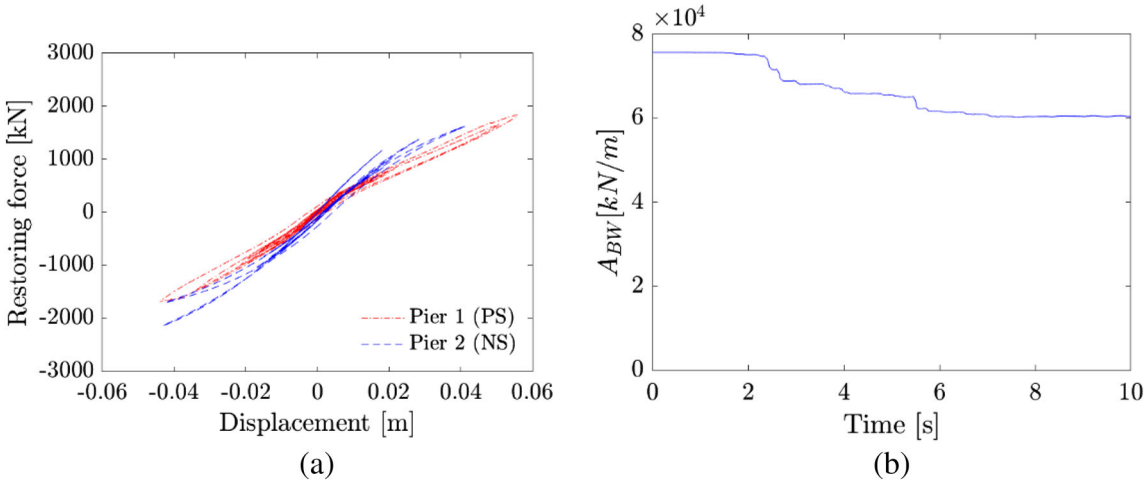

FIGURE 22 Test HT3-HE-60 with AB configuration: (a) hysteretic loops of restoring forces of both physical and numerical piers; (b) time history of the estimate of the Bouc-Wen parameter A_{BW} identified online by the UKF

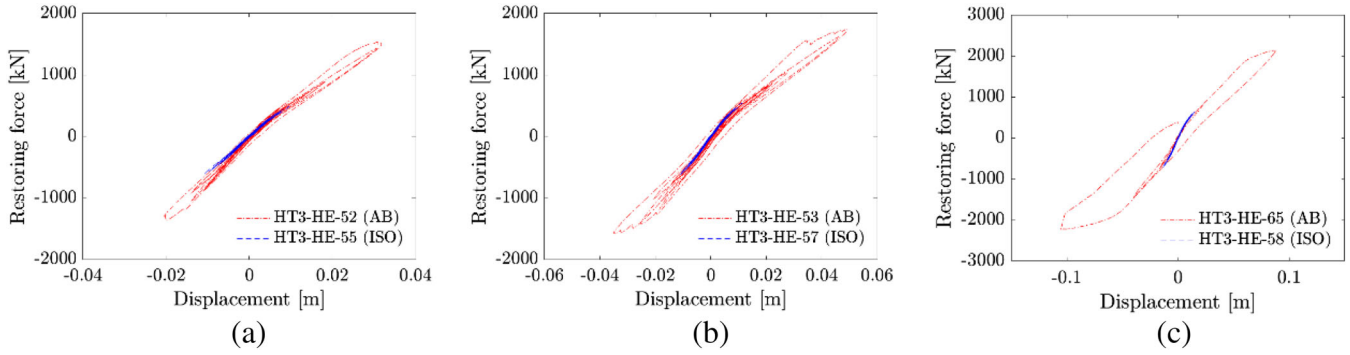

FIGURE 23 Comparison between hysteretic loops of the physical Pier #1 restoring force in both the AB and ISO #1 configurations at (a) PGA = 0.35 g, (b) PGA = 0.50 g, and (c) PGA = 0.75 g

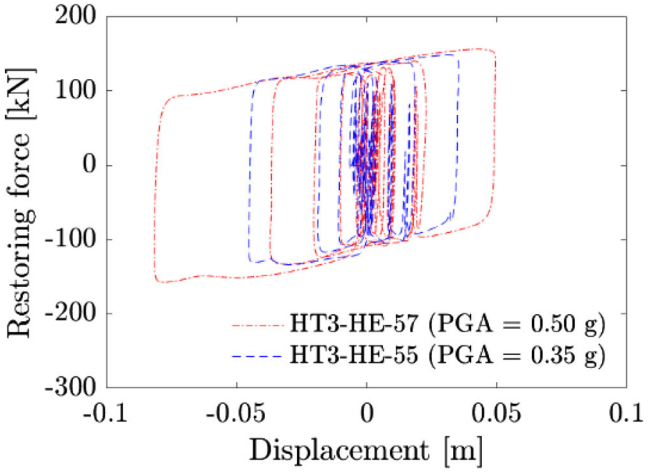

FIGURE 24 Hysteretic loop of the restoring force of the tested D-CSB

5 | CONCLUSIONS

According to the state of the art, monolithic time integration algorithms coordinate fast- and real-time hybrid simulation with online model updating. In detail, numerical substructures and dynamic identification models are evaluated within the same simulation loop, which is synchronized with the sampling rate of the control system. Such an approach does not allow for subsampling the numerical substructure response and the online estimation process associated with model updating, thus limiting the complexity of adopted computational models. This paper showed that partitioned time integration permits exploiting the parallelization capabilities of multi-core CPUs by splitting the hybrid simulation loop into multiple parallel processes with different sampling rates. The advantage is clear for the specific case of fast-time hybrid simulation, which still requires a hard real-time implementation strategy. In this case, both the numerical substructure and the online parameter estimation processes can be subsampled with respect to the control system sampling period. Although the experimental validation reported in the paper refers to the pseudodynamic regime, a hard real-time implementation approach was pursued, thus proving the validity of the proposed framework. As a final remark, we deem it important to stress that, more than the specific online estimation method, a plausible nonlinear model of the PS determines the feasibility of hybrid simulation with online updating. Therefore, both the sensitivity analysis of model parameters against observed response quantities as well as order reduction of identification models will drive our future research in this area.

ACKNOWLEDGEMENTS

The financial support from the Experimental Laboratory of EUCENTRE, Pavia, Italy, the STRIT project funded by the Italian Ministry of Education, University and Research (MIUR), and the RELUIS-DPC 2014–2018 project funded by the Italian Civil Protection Department is greatly appreciated. Moreover, the first author acknowledges the support of the Chair of Structural Dynamics and Earthquake Engineering (Prof. B. Stojadinovic) of ETH Zurich while the fourth author acknowledges funding from the Italian Ministry of Education, University and Research (MIUR) in the frame of the "Departments of Excellence" grant L. 232/2016 and the SERA grant agreement no. 730900.

ORCID

Giuseppe Abbiati https://orcid.org/0000-0002-5048-8505
Igor Lanese https://orcid.org/0000-0002-9716-0603
Saeed Eftekhar Azam https://orcid.org/0000-0001-8153-5506
Oreste S. Bursi https://orcid.org/0000-0003-3072-7414
Alberto Pavese https://orcid.org/0000-0003-4616-7693

REFERENCES

1. Calabrese A, Strano S, Terzo M. Real-time hybrid simulations vs shaking table tests: case study of a fibre-reinforced bearings isolated building under seismic loading. *Struct Control Health Monit*. 2015;22:535-556.
2. Schellenberg AH, Becker TC. Hybrid shake table testing method: theory, implementation and application to midlevel isolation. *Struct Control Health Monit*. 2016;24(5):e1915.
3. Pegon P, Pinto A. Pseudo-dynamic testing with substructuring at the ELSA Laboratory. *Earthq Eng Struct Dyn*. 2000;29(7):905-925.
4. Schellenberg AH, Mahin SA, Fenves GL. *PEER Report 2009/104. Advanced Implementation of Hybrid Simuation*. Berkeley: Pacific Earthquake Engineering Research (PEER) Center, University of California; 2009.
5. Kwon O-S, Kammula V. Model updating method for substructure pseudo-dynamic hybrid simulation. *Earthq Eng Struct Dyn*. 2013;42(13):1971-1984.
6. Hashemi MJ, Masroor A, Mosqueda G. Implementation of online model updating in hybrid simulation. *Earthq Eng Struct Dyn*. 2014;43(3):395-412.
7. Abbiati G, Bursi OS, Caperan P, Di Sarno L, Molina FJ. Hybrid simulation of a multi-span RC viaduct with plain bars and sliding bearings. *Earthq Eng Struct Dyn*. 2015;44(13):2221-2240.
8. Kalman RE. A new approach to linear filtering and prediction problems. *J Basic Eng*. 1960;82(1):35-45.
9. Julier SJ, Uhlmann JK. New extension of the Kalman filter to nonlinear systems. In: *Signal Processing, Sensor Fusion, and Target Recognition VI*. Vol.3068 International Society for Optics and Photonics; 1997:182-194.
10. Yang G, Wu B, Ou G, Wang Z, Dyke S. HyTest: platform for structural hybrid simulations with finite element model updating. *Adv Eng Softw*. 2017;112:200-210.
11. Mei Z, Wu B, Bursi OS, Yang G, Wang Z. Hybrid simulation of structural systems with online updating of concrete constitutive law parameters by unscented Kalman filter. *Struct Control Health Monit*. 2018;25(2):e2069.

12. Wu B, Chen Y, Xu G, Mei Z, Pan T. Hybrid simulation of steel frame structures with sectional model updating. *Earthq Eng Struct Dyn*. 2016;45(8):1251-1269.
13. Shao X, Mueller A, Mohammed BA. Real-time hybrid simulation with online model updating: methodology and implementation. *J Eng Mech*. 2015;142(2):04015074.
14. Schellenberg A, Mahin SA, Fenves GL. A software framework for hybrid simulation of large structural systems. In: *Structural Engineering Research Frontiers*; 2007:1-16.
15. Kwon OS, Nakata N, Elnashai A, Spencer B. Technical Note A framework for multi-site distributed simulation and application to complex structural systems. *J Earthq Eng*. 2005;9(5):741-753.
16. Shin KG, Ramanathan P. Real-time computing: a new discipline of computer science and engineering. *Proc IEEE*. 1994;82(1):6-24.
17. Song W, Dyke S. Real-time dynamic model updating of a hysteretic structural system. *J Struct Eng*. 2014;140(3):04013082.
18. MathWorks. MATLAB webpage, MathWorks, 7 2 2018. [Online]. Available: https://ch.mathworks.com/. [Accessed 7 2 2018].
19. Bonelli A, Bursi OS, He L, Magonette G, Pegon P. Convergence analysis of a parallel inter-field method for heterogeneous simulations with dynamic substructuring. *Int J Numer Methods Eng*. 2008;75(7):800-825.
20. Bursi OS, Abbiati G, Cazzador E, Pegon P, Molina FJ. Nonlinear heterogeneous dynamic substructuring and partitioned FETI time integration for the development of low-discrepancy simulation models. *Int J Numer Methods Eng*. 2017;112(9):1253-1291.
21. Abbiati G, Lanese I, Cazzador E, Bursi OS, Pavese A. A computational framework for fast-time hybrid simulation based on partitioned time integration and state-space modeling. *Struct Control Health Monit*. 2019:1-28.
22. Pegon P, Magonette G. *Technical Report 1.02.167 'Continuous PSD Testing With Nonlinear Substructuring: Presentation of a Stable Parallel Inter-field Procedure'*. Ispra, Italy: European Commission, Joint Research Centre, ELSA; 2002.
23. Brüls O, Arnold M. The generalized-α scheme as a linear multistep integrator: toward a general mechatronic simulator. *J Comput Nonlinear Dyn*. 2008;3(4):41007.
24. Brun M, Batti A, Combescure A, Gravouil A. External coupling software based on macro- and micro-time scales for explicit/implicit multi-time-step co-computations in structural dynamics. *Finite Elem Anal Des*. 2014;86:101-119.
25. Ismail M, Ikhouane F, Rodellar J. The hysteresis Bouc-Wen model, a survey. *Arch Comput Meth Eng*. 2009;16(2):161-188.
26. Mostaghel N. Analytical description of pinching, degrading hysteretic systems. *J Eng Mech*. 1999;2(216–224):125.
27. Chang S-Y. Error propagation in implicit pseudodynamic testing of nonlinear systems. *J Eng Mech*. 2005;131(2):1257-1269.
28. Chen C, Ricles JM. Tracking error-based servohydraulic actuator adaptive compensation for real-time hybrid simulation. *J Struct Eng*. 2010;136(4):432-440.
29. Mosqueda G, Stojadinovic B, Mahin SA. Real-time error monitoring for hybrid simulation. Part I: methodology and experimental verification. *J Struct Eng*. 2007;133(8):1100-1108.
30. Mosqueda G, Stojadinovic B, Mahin SA. Real-time error monitoring for hybrid simulation. Part II: structural response modification due to errors. *J Struct Eng*. 2007;133(8):1109-1117.
31. Ou G, Dyke SJ, Prakash A. Real time hybrid simulation with online model updating: an analysis of accuracy. *Mech Syst Signal Process*. 2017;84:223-240.
32. Peloso S, Pavese A, Casarotti C. Eucentre TREES Lab: laboratory for training and research in earthquake engineering and seismology. In: *Role of Seismic Testing Facilities in Performance-Based Earthquake Engineering*. Dordrecht: Springer Netherlands; 2012:65-81.
33. McKenna F. OpenSees: open system for earthquake engineering simulation. *Comput Sci Eng*. 2011;13(4):58-66.
34. Peloso S, Pavese A. "FRP seismic retrofit for insufficient lap-splice: large scale testing of rectangular hollow section bridge piers," in Proceedings of the ECCOMAS Thematic Conference on Computational Methods in Structural Dynamics and Earthquake Engineering (COMPDYN), Rhodes, Greece; 2009.
35. Chopra A. *Dynamics of Structures: Theory and Applications to Earthquake Engineering*. Saddle River, NJ: Prentice Hall. Inc.; 1995.
36. Iervolino I, Galasso C, Cosenza E. REXEL: computer aided record selection for code-based seismic structural analysis. *Bull Earthq Eng*. 2010;8(2):339-362.
37. Molina FJ, Magonette G, Pegon P, Zapico B. Monitoring damping in pseudo-dynamic tests. *J Earthq Eng*. 2011;15(6):877-900.
38. Furinghetti M, Pavese A, Quaglini V, Dubini P. Experimental investigation of the cyclic response of double curved surface sliders subjected to radial and bidirectional sliding motions. *Soil Dyn Earthq Eng*. 2019;117:190-202.
39. Pavese A, Furinghetti M, Casarotti C. Experimental assessment of the cyclic response of friction-based isolators under bidirectional motions. *Soil Dyn Earthq Eng*. 2018;114:1-11.
40. Fenz DM, Constantinou MC. Spherical sliding isolation bearings with adaptive behavior: theory. *Earthq Eng Struct Dyn*. 2008;37(2):163-183.

How to cite this article: Abbiati G, Lanese I, Eftekhar Azam S, Bursi OS, Pavese A. A framework for hybrid simulation with online model updating suitable for hard real-time computing. *Struct Control Health Monit*. 2020; e2652. https://doi.org/10.1002/stc.2652